# Friction stir welding of additively manufactured A20X aluminum alloy: welding process, mechanical properties, and microstructure

# Friction stir welding of additively manufactured A20X aluminum alloy: welding process, mechanical properties, and microstructure

# Friction stir welding of additively manufactured A20X aluminum alloy: welding process, mechanical properties, and microstructure

Mohammad Abankar[1], Vincenzo Lunetto[1,2]*, Manuela De Maddis[1,2], Pasquale Russo Spena[1,2]

[1]Department of Management and Production Engineering, Politecnico di Torino, Corso Duca degli Abruzzi 24, 10129 Torino, Italy

[2]Advanced Joining Technologies Laboratory (J-Tech@Polito), Politecnico di Torino, Corso Duca degli Abruzzi 24, 10129 Torino Italy

* Corresponding author

Email: vincenzo.lunetto@polito.it

## Abstract

A20X is an advanced and high-strength additive manufacturing aluminum alloy with promising applications in several fields, including aerospace and aeronautics. However, its assembling through fusion welding technologies poses challenges due to the detrimental effects of melting and solidification. Friction stir welding offers a promising solution for joining A20X, producing components with superior mechanical properties while preserving the engineered microstructures. This study investigates the influence of friction stir welding on the quality of butt joints made of 4 mm thick additively manufactured A20X plates produced by laser powder bed fusion. Different rotational (900 and 1500 rpm) and welding speeds (100 and 500 mm/min) were tested to evaluate the influence of the joining process on weld quality (mechanical strength, microstructures, welding defects, and surface roughness). Friction stir welding maintains a very fine microstructure in the welds, with only a slight reduction of the mechanical strength compared to the base material (335 MPa vs. 385 MPa on average). The hardness of the welded joints increases, likely due to local aging caused by the heat input during the joining process. Lower tool rotation and welding speed result in tunnel defects, notably reducing joint strength. 3D X-ray computed tomography reveals that the metal stirring occurring during the joining process notably reduces the intrinsic porosity of A20X. It also breaks up Ti borides and promotes the growth of Al-Cu precipitates within the stir zone. The fractographic analysis highlights the ductile behavior of A20X after welding, emphasizing the critical role of welding parameters in joint integrity.

Keywords: Friction Stir Welding, Additively manufactured A20X, 3D X-ray tomography, Mechanical strength, Microstructure, Tunnel defect.

## 1. Introduction

Aluminum alloys are highly attractive for lightweight engineering applications in the automotive, aerospace, and automotive fields due to their high specific strength and toughness. In recent years, the advent of additive manufacturing has opened new potentials for these alloys, enabling the fabrication of components with intricate geometries that are challenging to achieve using conventional manufacturing techniques. In this context, laser powder-bed fusion (LPBF) technology has emerged as a pivotal method for producing high-strength aluminum alloys with complex shapes to fulfill the growing industry demand. Several aluminum alloys, such as Al-Si [1,2], AlSi10Mg [3,4], Scalmalloy® [5], and A20X [6], have been effectively produced via LPBF. The LPBF

aluminum alloys most frequently used are based on Al-Si casting alloys. These alloys are characterized by enhanced mechanical properties when compared to traditional Al-Si cast alloys [1,2]. Al-Si alloys processed through LPBF exhibit good printability, attributed to their eutectic Si phase, alongside a narrow solidification range that prevents the risk of solidification cracking [7]. LPBF AlSi10Mg has gained significant interest from the research community [3,4] due to its broad range of industrial applications and noteworthy yield strength. This alloy features a cellular microstructure consisting of primary α-Al cells (Figure 1 a)) with $Mg_2Si$ precipitates and Si eutectic phase [3]. $Mg_2Si$ precipitates in the AlSi10Mg alloy hamper dislocation movement, enhancing mechanical strength [3]. Furthermore, the formation of large columnar grains oriented along the heat transfer direction imparts anisotropic mechanical properties to the Al-SiMg alloys [7]. Figure 2 summarizes the yield strength for as-built AlSi10Mg alloys as found in the literature. The yield strength is the range of 150 - 300 MPa for most LPBF Al-Si alloys [8], with certain aging conditions providing higher values between 275 and 325 MPa [9,10]. However, the relatively low yield strength and anisotropic mechanical properties of the Al-Si alloy system [8] do not meet the growing demand for high-strength alloys with isotropic properties. This challenge has spurred significant efforts in developing an advanced generation of aluminum alloys. In particular, the non-heat-treatable 5xxx series has been enhanced to become precipitation-hardened Al alloys through the addition of peculiar elements, such as Sc and Zr [5,11,12]. The introduction of small amounts of Sc and Zr leads to the formation of $Al_3$(Sc, Zr) particles, acting as dispersoids that improve mechanical performance. This addition notably reduces the size of columnar grains, largely modifying microstructure into submicron equiaxed grains [8]. Such transformation remarkably shifts the mechanical behavior from anisotropic to isotropic [7]. LPBF additively manufactured (AM) Al-Mg-Sc-Zr grade, also known as the trade name Scalmalloy®, represents a new generation within the Al-Mg alloys, featuring a bi-modal microstructure with fine and uniformly dispersed $Al_3$(Sc, Zr) particles in the α-aluminum microstructure [8]. The typical microstructure of LPBF Scalmalloy® is shown in Figure 1 b) [5]. $Al_3$(Sc, Zr) particles enhance mechanical strength, even at high temperatures [13]. The yield strength of Scalmalloy® usually ranges between 250 and 350 MPa, Figure 2. Therefore, LPBF Al-Mg-Sc-Zr alloys are positioned to supersede traditional AM alloys like AlSi10Mg, AlSi7Mg, and AlSi12, offering superior thermal stability and yield strength [14]. However, both Al-Si alloys and Scalmalloy® have limited anisotropic mechanical properties, which can restrict their application fields [15].

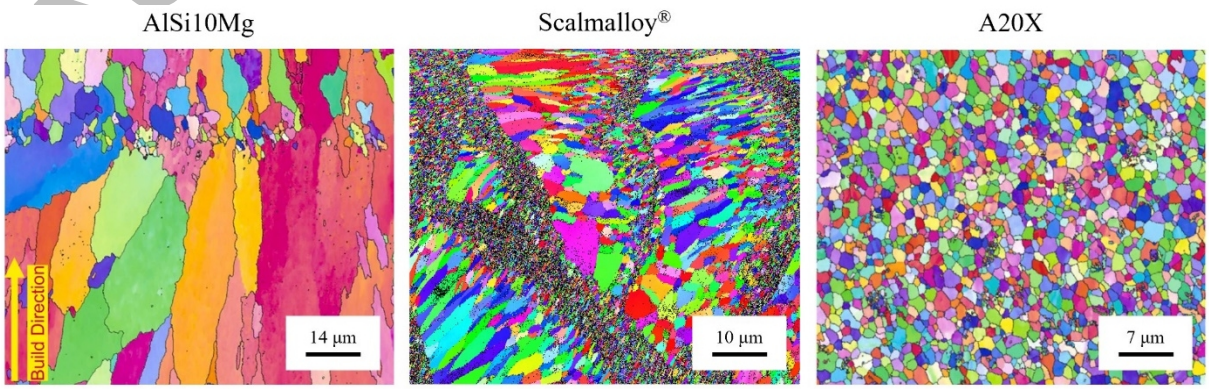


Figure 1. EBSD map of LPBF a) AlSi10Mg showing columnar grains along the build direction and some equiaxed grains with no specific preferred orientation [3], b) Scalmalloy® with bi-modal microstructure [5] and c) A20X with equiaxed grains [16].

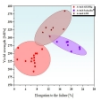

Figure 2. Yield strength and elongation of LPBF AlSi10Mg, Scalmalloy®, and A20X. See the supplement table for details.

LPBF A20X has emerged as a novel high-strength Al-Cu-Mg-Ag alloy, characterized by a homogeneous and texture-free microstructure of α-aluminum reinforced with $TiB_2$ [6,16] and $Al_2Cu$ precipitates within grains and along grain boundaries [17,18]. The grains in an as-built A20X are relatively small and equiaxed, Figure 1 c), contrasting with the typical epitaxial growth observed in Al-Si system alloys [6] or the bi-modal feature of Scalmalloy® [5]. This difference is attributed to $TiB_2$ particles being more effective grain refiners than $Al_3$(Sc, Zr) because of higher coherency with the matrix lattice [8]. Ghoncheh et al. [19] have reported A20X to exhibit quasi-isotropic mechanical behavior owing to fine and equiaxed grains without a strong preferential crystallographic orientation along any direction. The thermal stability (max operating temperatures at least 50 °C higher than the limits of conventional aluminum alloys) and versatility of LPBF A20X make it suitable for high-temperature applications [18].

The chemical composition of A20X alloy includes Al, Ag, Mg, Cu, Si, Ti, and B, each playing a unique role in the alloy strengthening. Cu can be both dissolved in the matrix as a solid solution and as $Al_2Cu$ precipitates within the grains and/or along grain boundaries [6]. Li et al. [6] have shown that the rapid cooling rate associated with LPBF leads to Cu becoming supersaturated within the α-Al grains. Subsequent repeated laser heating cycles, approximately at 150°C (close to the aging temperature of around 170°C), provide an in-situ aging environment for A20X alloy, mitigating the mismatch of $TiB_2$/aluminum interface. Laser heating lowers the nucleation energy barrier and shortens the diffusion path for vacancies and solute atoms during aging, facilitating heterogeneous precipitation. Although the Ω and $\theta''/\theta'$ precipitates typically result from solubilization and subsequent aging [20], they are still detectable in the as-built A20X microstructure. However, a tailored post-heat-treatment can enhance the strengthening effect, improving mechanical properties in the as-built parts [3]. Ag is an efficient trap for Mg atoms, leading to the formation of Mg-Ag co-clusters on the {111} planes. These co-clusters also serve as heterogeneous nucleation sites for Ω-$Al_2Cu$ precipitates [20]. The addition of Ag in Al–Cu–Mg alloys promotes dense precipitation of the Ω phase while inhibiting the θ′ phase. The dense Ω-$Al_2Cu$ precipitates are the most effective strengthening phases in A20X

at both room and high temperatures [20]. This effect is attributed to the fact that {111} plane is the main glide plane in the Al face-center cubic matrix, where hexagonal-shaped plate-like Ω-$Al_2Cu$ precipitates effectively impede dislocation glide, thereby reinforcing the A20X alloy [3,18,20].

The high strength and the great thermal stability make additively manufactured A20X alloy a promising solution for applications in the aeronautic and aerospace industries (e.g., satellite parts). However, the widespread use of this alloy also requires its assembling with other parts. Laser welding is often a solution for joining engineered components due to its ability to minimize residual stresses, distortion, and the heat-affected areas. Despite this, fusion welding technologies pose significant challenges due to the detrimental effect of melting and solidification, which alter the engineered structures of the additive parts. The high heat inputs coarsen AM microstructure and eliminate some of the beneficial effects of the rapidly solidified structure achieved during layer-by-layer manufacturing. Moreover, LPBF has limitations in building large components. Other AM techniques, such as direct energy deposition (DED), can address this issue but the low superficial detail resolution may result in coarser surfaces that typically need post-processing to meet acceptable surface finishes [21]. Electron beam melting (EBM) may have limitations in terms of material availability, dimensional accuracy, and surface finish compared to LPBF [22]. However, some major challenges remain in the AM of large-scale high-strength aluminum alloy components, especially with printability, defect control, and low production volume with commercial off-the-shelf machines [23].

Friction stir welding (FSW) offers a promising solution for joining additively manufactured A20X, producing assembled components with superior mechanical properties while preserving the engineered microstructures [5]. This solid-state joining technique mitigates common issues associated with traditional fusion welding methods (e.g., laser and arc welding), such as heat affected zones, residual stresses, and thermal distortions. Additionally, FSW retains the benefits of the rapidly solidified A20X structure from the additive production, including a very fine grain size and supersaturated solid solution. As a result, a single high-temperature aging treatment can be conducted after the additive fabrication to achieve both stress-relieving and strengthening [8]. Currently, there are no studies specifically about the welding of A20X alloy and the influences of the joining process on weld quality. However, several studies have already demonstrated that friction stir welding enhances the corrosion resistance of advanced aluminum alloys [24,25]. The advantages of solid-state joining have also attracted the interest among additive manufacturing researchers to explore the production of components via friction stir additive manufacturing [26,27].

This study investigates the influence of FSW on the mechanical and microstructural properties of A20X obtained via LPBF at varying welding conditions (i.e., different rotation and welding speeds). The welding parameters, including tool spindle torque and vertical and advancing forces, were monitored in real-time to provide a comprehensive understanding of the joining process. The microstructure of the FSW joints was assessed via optical microscopy, while the mechanical properties were evaluated through hardness and tensile tests. 3D X-ray Computed Tomography was carried out to detect the porosity and welding defects in the as-printed A20X and after welding to assess joint quality. Finally, a fractographic examination was also conducted

on the fracture surfaces of the welded tensile samples to assess the fracture modes under the different welding conditions.

## 2. Materials and methods

A20X plates measuring 4 mm thick, 75 mm long, and 55 mm wide were produced via LPBF technology. According to the technical datasheet, Table 1 reports the chemical composition of the A20X powder. The powder size distribution ranges from 20 to 63 µm. The parameters for the metal printing process included a laser power of 370 W and a layer thickness of 30 µm. The average density of as-printed A20X was 99.7 %. All plates had their length parallel to the build direction. The average surface roughness of the A20X coupons was characterized by Ra = 4.1 µm, Rt = 31.3 µm, and Rz 23.7 µm.

Table 1. Chemical composition (wt.%) of A20X, as from the supplier technical datasheet.

| wt.% | *Cu* | *Si* | *Mg* | *B* | *Ag* | *Ti* | *Fe* | *Al* |
|---|---|---|---|---|---|---|---|---|
| | 4.2 to 5.0 | 0.1 max | 0.20 to 0.33 | 1.25 to 1.55 | 0.6 to 0.9 | 3.00 to 3.85 | 0.08 max | bal. |

A preliminary experimental campaign was conducted to identify the process parameters suitable for obtaining proper joints, including plunge depth, plunge speed, dwell time, welding, and rotational speeds. The process parameters for the FSW campaign on the AM plates are reported in Table 2. The welding tests were performed using an FSW machine (Stirtec GmbH, mod. FSW100) with a nominal capacity of 100 kN in vertical force and 600 Nm in torque, equipped with a water-cooled spindle, Figure 3 a). The FSW tool was made of S705 high-speed steel (alloyed with Co, Mo, Cr, V, and W) in the quenching and tempering condition and hardness of 65 HRC, Figure 3 b). The tool had a 12 mm flat scrolled shoulder to promote metal stirring. The spiral groove on the scrolled shoulder was 0.4 mm wide and 0.2 mm deep. The shoulder ended with a 4 mm truncated conical pin with a screwed surface and a cone angle of 15º. Two nozzles, positioned at the front and rear of the FSW tool, fed an argon shielding gas to protect the weld from oxidation.

Table 2. Process parameters for the FSW campaign on the A20X plates.

| Tilt angle [°] | Plunge depth [mm] | Plunge speed [mm/min] | Dwell time [s] | Welding speed [mm/min] | Rotation speed [rpm] |
|---|---|---|---|---|---|
| 2 | 4 | 10 | 2 | 100, 500 | 900, 1500 |

a) b)

Figure 3. a) FSW equipment and b) tool geometry used for the welding tests (dimensions in [mm]).

Five tensile samples were obtained from the welded coupons using wire electro-discharge machining (Baoma, mod. BMW-3000) for mechanical testing, and four samples for microstructural examination, Figure 4. At varying welding conditions, the samples were labeled using the nomenclature Vx-wy, where "V" means welding speed, "w" rotational speed, and x and y are their values, respectively. The mechanical strength of the FSW joints was assessed through tensile tests (ZwickRoell, mod. Z050) on dogbone samples according to ISO 6892 standard [28]. These trials were conducted on a standard testing machine, operating at a crosshead speed of 10 mm/min. The cross-sections of the FSW joints were examined using optical microscopy (Carl Zeiss, mod. Axio Vert A1). The preparation of the metallographic samples followed a standard procedure involving grinding, polishing, and a final chemical etching with Keller's reagent. Scanning electron microscopy (Tesca, mod. MIRA3 XMH), SEM, was used to evaluate the fracture surfaces of the welded joints. The joint appearance was assessed through visual examination and surface roughness measurements.

Figure 4. Sketch of the FSW welds, tensile, and metallographic samples.

The hardness of both the as-printed and as-welded samples was evaluated throughout their joint cross-section using Vickers hardness testing. The tests (Innovatest, mod. Nova 130) were conducted according to the ASTM E92 standard [29], using a 500 g load, dwell time of 15 s, and a spacing distance of 1 mm between two successive indentations. Vickers hardness maps were generated with MATLAB software for detailed analysis. 3D X-ray Computed Tomography was conducted to detect the size, shape, and distribution of porosity and possible defects in the as-printed A20X coupons. The same test was repeated on the same samples after FSW welding. The nondestructive tests were performed using 300 kV tomographic equipment (customized tomography machine from Fraunhofer IKTS) with a maximum resolution of 5 µm. The system was equipped with a 4-axis worktable enabling precise manipulation of the sample in the x-y-z directions and allowing for a continuous 360° rotation. The welded samples were examined with 210 kV voltage and 60 mA current, with the sample undergoing incremental rotations of 0.225°. Four projections were acquired for each incremental rotation and recorded as the reference for that specific position. A total of 1600 projections were collected over a full 360° rotation for the 3D reconstruction of the sample. The data were processed by VGSTUDIO software. The VGDefX algorithm was used to have detailed information about porosity and defects. The sphericity parameter ($\Psi$) of the detected features was computed with Eq. (1), according to Wadell [30]. Pore sphericity is defined as the ratio between the surface area of a sphere ($A_S$) with the same volume as the pore ($V_P$) and the effective surface area of the pore ($A_P$). Moreover, the volume of the pore ($V_P$) can be used to calculate the equivalent diameter of a pore ($d_{Eq}$), as defined in Eq. (2). The analysis achieved an image resolution of 15 µm, which is crucial for the capability of the VGDefX algorithm to detect pores and defects. The algorithm could not detect pores smaller than four times the volume of a cube with sides equal to the resolution. Therefore, the minimum pore volume targeted in this study was set to eight times

the volume of such a voxel, equating to 3375 µm$^3$. Based on this and Eq. (2), the minimum equivalent pore diameter is 37 µm.

$$\Psi = \frac{A_S}{A_P} = \frac{\pi^{1/3}\,(6 \bullet V_P)^{2/3}}{A_P} \tag{1}$$

$$d_{Eq} = 2 \bullet \sqrt[3]{\frac{3 \bullet V_P}{4 \bullet \pi}} \tag{2}$$

Figure 5 provides an overview of the methodology used in this work for the microstructural and mechanical characterization of FSW joints obtained under different welding conditions.

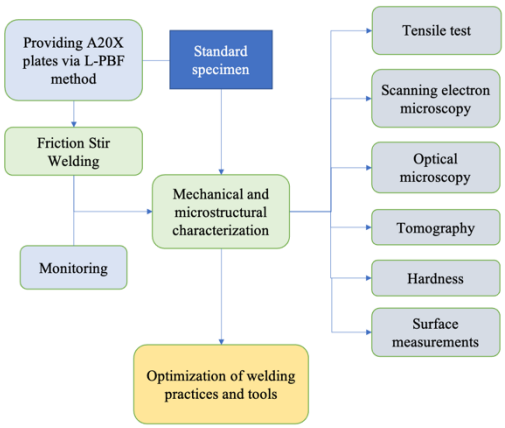


Figure 5. The research flow chart outlines of the friction stir welding for joining AM A20X plates and the different analyses performed on the resulting joints.

## 3. Results and discussion

### 3.1 FSW process parameters

Mishra et al. [31] pointed out the paramount importance of in-line monitoring of the FSW process. Their review emphasized that force and torque are sensitive indicators for detecting the material resistance to stirring and potential defects and, hence, give some indications about the effectiveness of metal plasticization and joint quality. In this context, Figure 6 shows the typical torque and tool forces (in both advancing and vertical directions) monitored during the FSW of A20X at varying welding and rotational speeds. During the plunge phase, the monitored curves have the same trend at a given rotation speed. An initial peak in vertical force around 5-6 kN is observed at 900 rpm, attributed to the attempt of the pin to penetrate the upper plates, Figure 6 a). At a higher rotational speed of 1500 rpm, the peak force is reduced to 4 kN because of the greater metal softening. As the tool plunges, the vertical force drops to around 2-3 kN, before increasing steadily until the shoulder touches the upper plates (3.8 mm of the plunge depth in approximately 22.8 s). The force increases again at 24 s with a plunge depth of 4 mm. The period from 24 s to 26 s marks the dwell phase associated with metal softening because of tool friction: the vertical force reduces to 4 kN at 900 rpm and 2 kN at 1500 rpm. The welding phase is affected by both the welding and rotational speeds. It lasts approximately 36 s and 7 s at

100 and 500 mm/min, respectively. A welding speed of 100 mm/min results in a decreasing trend of the vertical force, whereas a speed of 500 mm/min sees the vertical force peaking at 6 kN as the tool progressively encounters colder material. The welding speed notably influences the vertical force: it remains constant at 2-3 kN at 100 mm/min but increases to 4 kN at 500 mm/min. Spindle torque exhibits an uneven but monotonic increase throughout the welding cycle at 500 mm/min, while maintaining a nearly constant value at 100 mm/min. Overall, the torque increased with higher welding and rotational speeds: about 15-17 Nm at 900 rpm and 10-14 Nm at 1500 rpm.

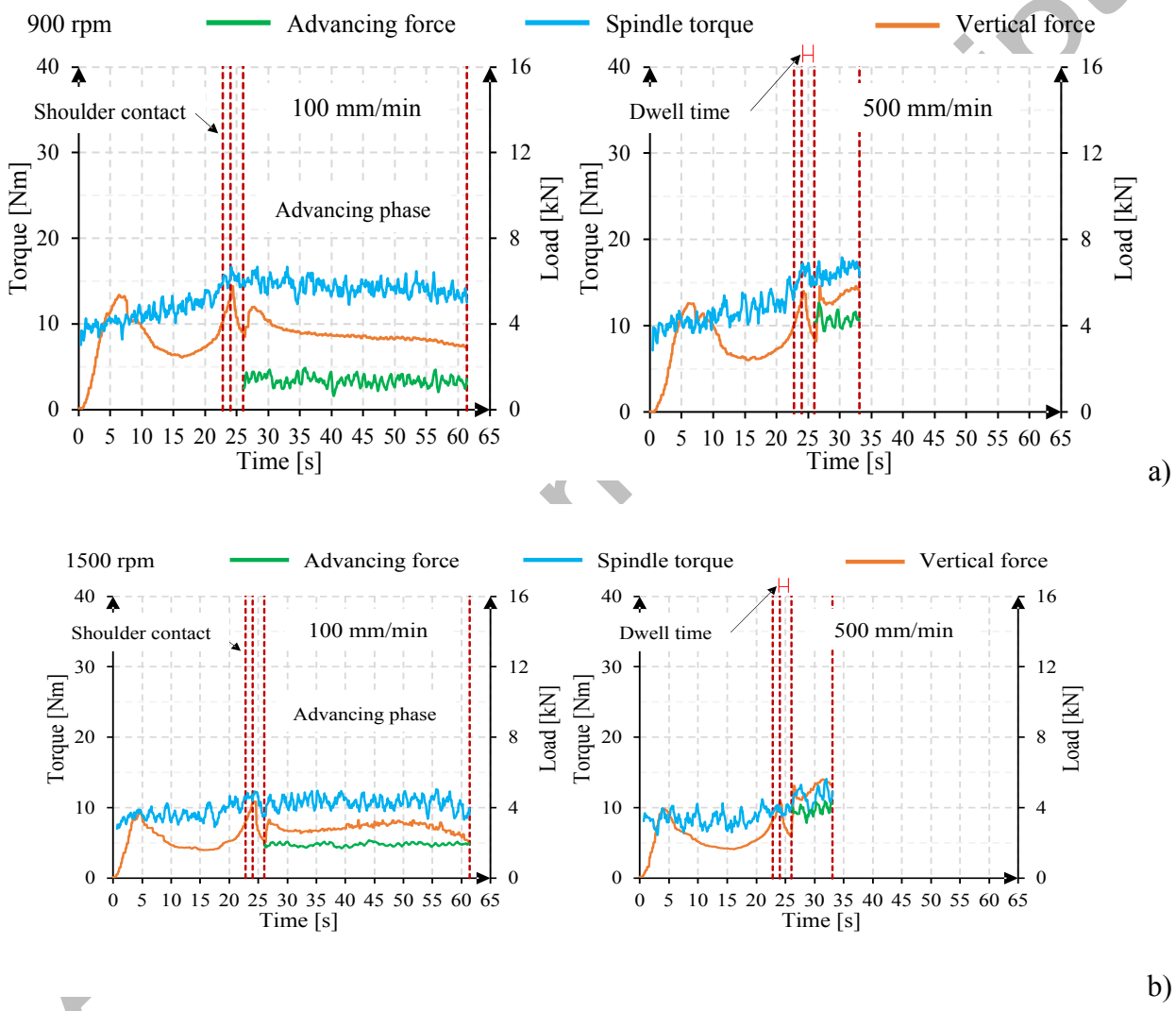


Figure 6. Monitored spindle torque, advancing and vertical forces during the FSW of A20X: a) rotational speed of 900 rpm, welding speed of 100 and 500 mm/min; b) rotational speed of 1500 rpm, welding speed of 100 and 500 mm/min.

Higher torque and forces are an indication of insufficient heat inputs involved during FSW. As discussed later, tunnel defects and rougher weld surfaces result from such improper heat input and, hence, metal stirring. These findings align with the research by Su et al. [32] about the FSW of AA2024-T4. They reported that the higher the rotational speed the lower the torque, and the higher the welding speed the higher the advancing force. They also emphasize that the vertical force is remarkably larger than the advancing force, as also found by

Mirandola et al. [5]. The torque and force data display that metal plasticization might be insufficient at the higher welding speed of 500 mm/min.

### 3.2 Microstructure and hardness examinations

Surface roughness affects the behavior of metals in different ways. For instance, a rougher surface increases stress concentration on the weldment surface, which can reduce mechanical strength, particularly under fatigue loading, and accelerate corrosion phenomena [33]. Therefore, after each friction stir welding experiment, the average surface roughness - measured as Ra, Rz, and Rt - was determined at the center of the weldment surface along the welding direction. The roughness data are integrated in Figure 7, which shows the appearance of FSW joints at varying welding conditions. Despite variations in these welding parameters, the joint width remains unchanged since it is mainly influenced by the shoulder diameter and plunge depth, which were kept fixed in this study (Table 2). This figure also reveals the formation of circular marks on the weldment surfaces, a consequence of the material flow below the tool shoulder during its revolution. Notably, smoother and more uniform welding seams result from reduced welding and increased rotational speeds. The influence on the weld surface roughness is more pronounced with variations in welding speed [34]: clear shoulder marks appear in the samples welded at 500 mm/min, which are associated with the highest roughness values. This phenomenon is attributed to the different thermal and material flow histories experienced across the joints: the joints welded at 100 mm/min are associated with higher heat inputs (i.e., high rotation and low welding speeds), experiencing a larger metal softening and plastic deformation. In this case, the surface roughness of the welds is lower than that of the as-built A20X (Ra 1.6-2.6 µm vs. 4.1 µm). Contrarily, the lower heat input and plasticity produced at 500 mm/min result in rougher surfaces with visible marks, leading to a higher surface roughness than the as-built A20X (Ra 4.9-6.0 µm vs. 4.1 µm). The results obtained are coherent with what has been found in the literature. For example, Bozkurt [34] reported an average surface roughness, Ra, of aluminum FSW joints (rotational speed 450 rpm and welding speed 40 mm/min) lower than 6 µm under optimal welding setting.

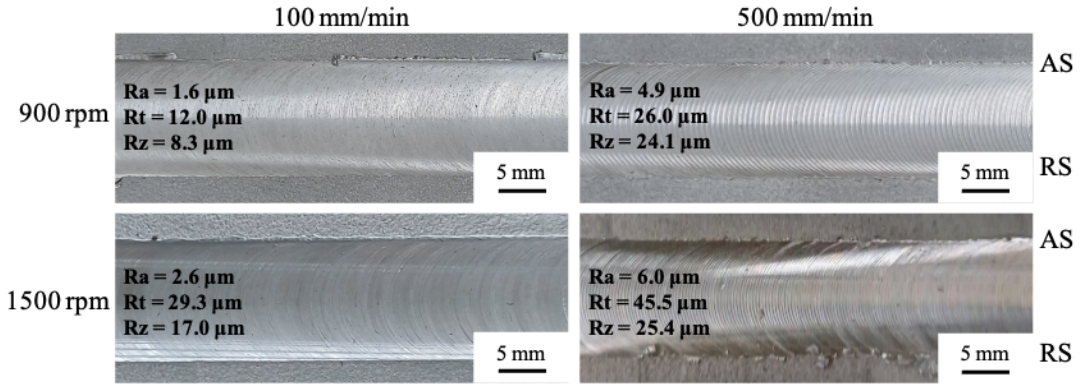


Figure 7. Appearance of the FSW joints at varying welding and rotational speeds. AS = advancing side; RS = retracting side. As a comparison, the roughness of additively A20X exhibits Ra = 4.1 µm, Rt = 31.3 µm, and Rz 23.7 µm.

Figure 8 depicts the typical cross-sections of FSW joints processed under different process parameters, highlighting the stir zone (SZ) and base material (BM). These regions were identified through a detailed analysis involving macrographs, hardness maps, and tool dimensions. As well-known, the metal stirring induces an asymmetric material flow at the advancing (AS) and retreating (RS) sides of the joint, giving the typical appearance in the FSW welds. The stronger material flow at the AS makes more evident the transition between the SZ and the thermomechanically affected zone (TMAZ), and heat affected zone (HAZ), while it is less detectable on the RS side. Moeini et al. [35] also reported a smooth transition from the BM to SZ on the retreating, while a clear interface between the BM and the SZ on the AS. The asymmetric nature of the FSW process makes the transition between affected regions on the AS and the SZ more evident. The material flow on the RS is less intense because the rotation direction is opposite to the welding direction and counteracts each other, while on the AS, the welding direction and rotation direction are the same. This leads to an increase in temperature and intense plastic deformation in the AS compared to the RS [36]. Onion rings (OR) form in all the welded samples, except under the V100-w1500 welding condition. Onion rings are generally the result of a metal stirring that involves a shear deformation within the SZ [37], remaining as marks of the material flow within the FSW weld [38]. They are often more evident at the AS because of the stronger plastic deformation at this side of the weld. OR-like formations in the SZ are an indication of a near-optimal plasticization, mixing, and coalescence of the material [39]. As the metal is strongly softened by a proper heat input (i.e., high rotation and low welding speeds), the tool homogeneously stirs the metals, and the resulting marks of such mix, and hence ORs, tend to disappear. This is because ORs are not observed under the V100-w1500 welding condition, since is associated with the maximum heat input developed during welding among the examined conditions.

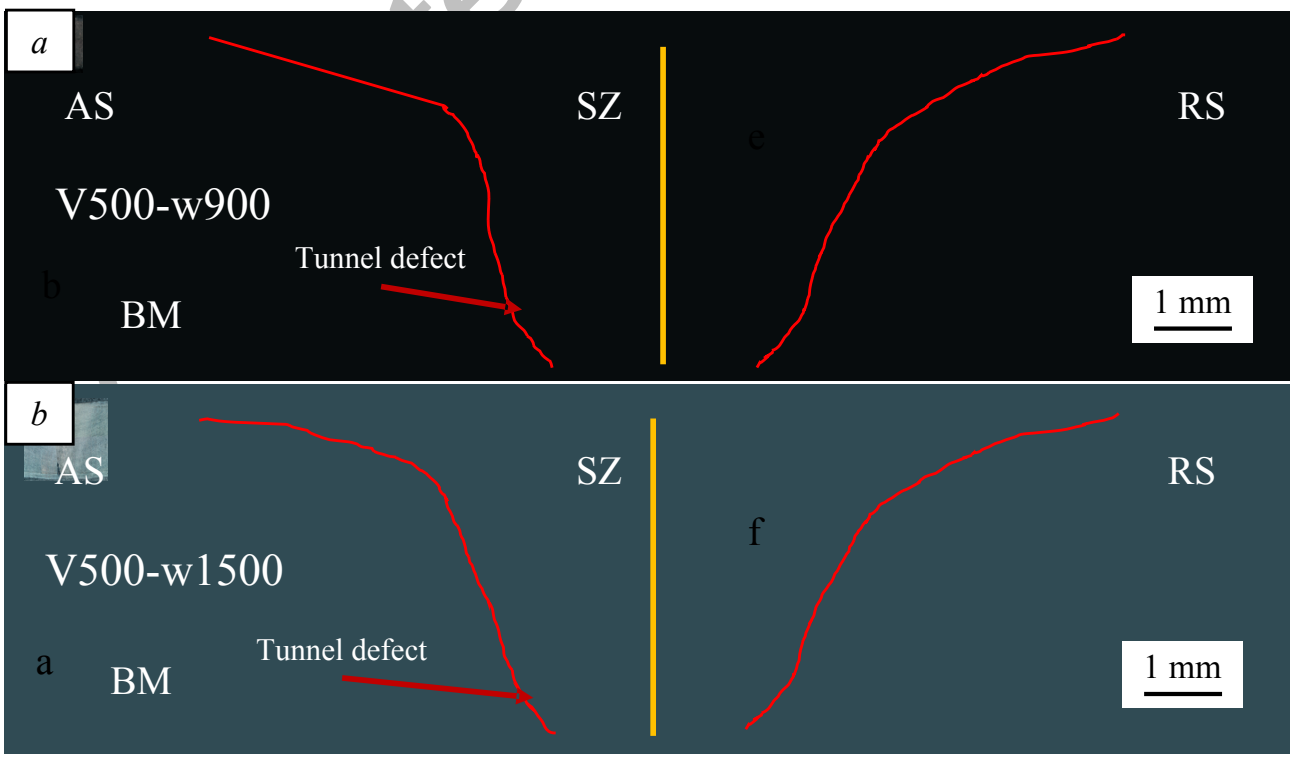

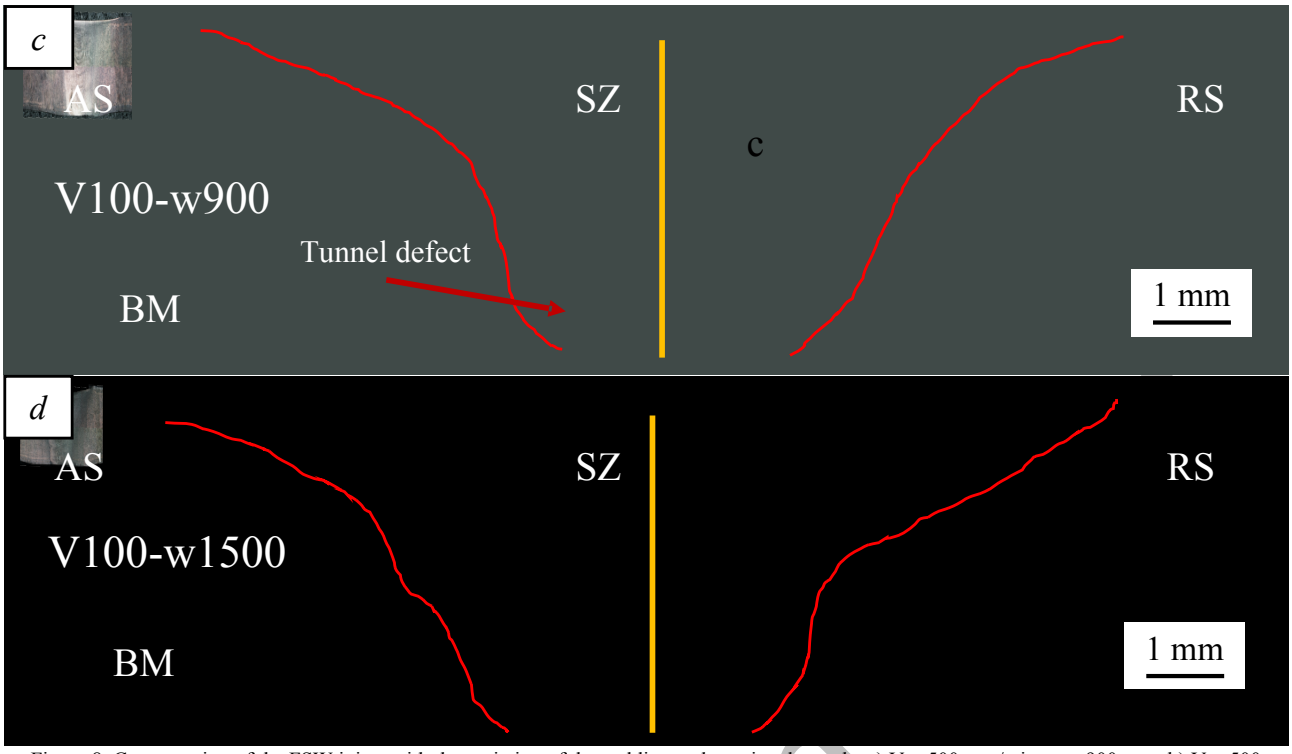


Figure 8. Cross-section of the FSW joints with the variation of the welding and rotational speeds: a) V = 500 mm/min, w = 900 rpm, b) V = 500 mm/min, w = 1500 rpm, c) V = 100 mm/min, w = 900 rpm, and d) V = 100, w = 1500 rpm. The numbered marks highlight the locations of the microstructures reported in Figure 9.

The extent of the SZ from the plate surface is consistently about 12 mm across all joints, a dimension mainly affected by the shoulder geometry and plunge depth, as detailed in Table 2. The width of the welding zone narrows toward the joint root, forming a conical shape influenced by heat input generated from friction and plastic flow below the shoulder, which increases with welding speed. The average width of the SZ at joint center measures 5.6 mm and 4.6 mm at 100 mm/min and 500 mm/min welding speeds, respectively. Joints welded at the same welding speed but with different rotational speeds exhibit similar SZ dimensions at the joint center, indicating that welding speed predominantly determines the SZ geometry at the joint root, the SZ narrows to 3.2 mm and 2.6 mm for welding speeds of 100 and 500 mm/min, respectively. The metallographic examination has pointed out tunnel defects in the welded samples. As shown in Figure 8, tunnel defects always occur when joining with the highest welding speed, namely V500-w900 and V500-w1500 samples, while they are discontinuous throughout the weldments for the samples V100-w900. Conversely, the tunnel is completely absent in the V100-w1500 samples. Tunnel is a defect in FSW that remarkably affects the mechanical properties of welded joints. An improper selection of welding process parameters, i.e., high welding and low rotation speeds, and/or tool design causes insufficient metal softening and plasticization, along with an unbalanced material flow around the tool pin [40]. As a result, insufficient metal stirring causes the formation of a tunnel defect throughout the weldment length [41]. Therefore, a proper heat input, and hence metal stirring, was developed when welding with the highest rotation and lowest welding speeds (V100-w1500 samples), but not for the V500-w900 and V500-w1500 samples welded. V100-w900 samples, instead, were joined under a critical welding condition associated with an intermediate heat input, which led to a discontinuous tunnel throughout the weldments. So, even though high welding speeds could be preferred to increase welding

productivity [40], lower welding speeds ensure proper heat inputs, with stronger metal stirring, and improved joint integrity [42,43]. This is particularly important for components subjected to significant stresses under the service [44]. The average cross-section of the tunnel defects is 0.406 $mm^2$ for the V500-w900 joint, 0.238 $mm^2$ for the V500-w1500 joint, and 0.15 $mm^2$ for the V100-w900 joint when this defect occurs. No further analysis was conducted on the V500-w900 samples due to the formation of a large and continuous tunnel defect. The location of the tunnel defect changes at varying heat input. In the V500-w900 (Figure 8 a)) and V100-w900 (Figure 8 c)) joints, which experienced the lowest heat inputs, the tunnel defect is inside the SZ. It is located at the AS in correspondence with the groove valleys of the threaded pin (Figure 3 b). At increasing heat input, the tunnel moves at first toward the border of the tool tip, V500-w1500 (Figure 8 b)), and then disappears when the joints experience proper heat inputs and metal stirring, V100-w1500 (Figure 8 d)).

Figure 9 a) and b) show the microstructures of the BM of the as-printed A20X and Figures 9 c), d), e), and f) show FSW joints at varying welding and rotational speeds. The letters are representative of the corresponding locations indicated in Figure 8. The LPBF process achieved a highly densified structure. Examination of weld cross-sections at macroscopic and microscopic scales reveals a nearly porosity-free microstructure within the SZ of the weld. The BM, marked by a, shows the marks of the laser scanning track. As shown in Figure 9 b), upon superior magnification, this microstructure features ultra-fine grains with an average grain size lower than 1 μm. In the SZs, the grain size remains quite small, showing little variation despite the significant changes in process parameters. This uniform microstructural transition from the BM to the SZ has never been highlighted in FSW joints of other AM aluminum alloys [38]. Moeini et al. [35] and Scherillo et al. [38] have found that FSW significantly alters the typical layer-by-layer microstructural morphology as-printed AlSi10Mg alloys, achieving substantial grain refinement in the SZ compared to the BM (about 70 times smaller). The reason is attributed to the severe plastic deformation (metal stirring) caused by the tool pin rotation, which promotes a dynamic recrystallization (DRX) [45] with a consequent remarkable grain refinement [45]. Figure 9 displays that the as-built A20X has relatively small and equiaxed grains, which differ from the typical columnar grains of AlSi10Mg alloy [6] and the bi-modal microstructure of Al-Sc-Zn Scalmalloy® [5]. This distinction is attributed to the $TiB_2$ particles, which have an effective grain refinement capability due to the high coherency with the α-aluminum crystal lattice [8]. Moreover, Ti dissolution in the melt promotes the formation of $Al_3Ti$ layers on the $TiB_2$ particles, which enhance the nucleation of α-aluminum through peritectic reactions [18,20,46,47]. As a result, the as-built A20X exhibits very fine and equiaxed grains without any preferred texture [19], maintaining a consistent grain size between SZ and the BM in the joined A20X plates.

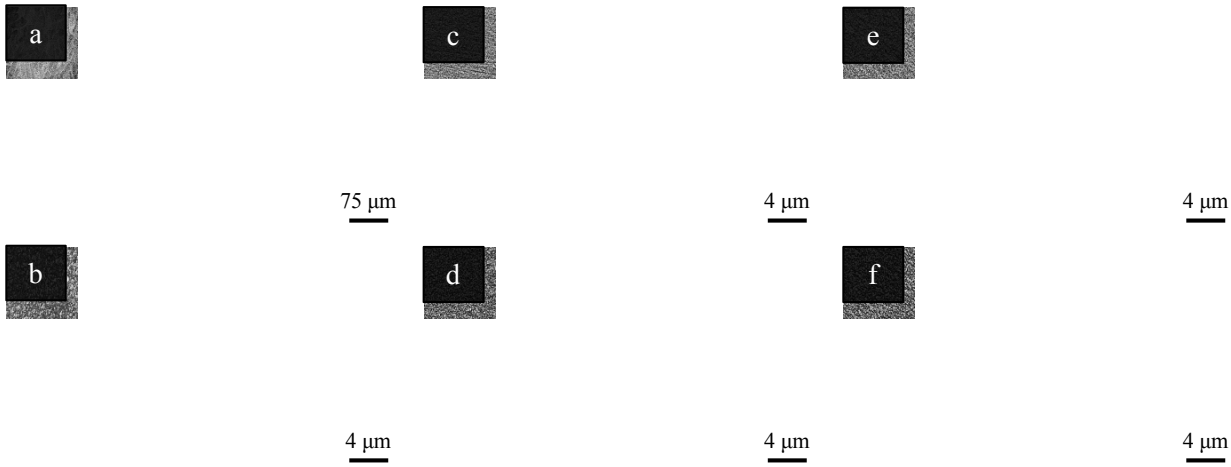


Figure 9. The optical microscopy images of a) base material with signs of scanning tracks, b) base material microstructure, c) stir zone of V100-w900 joint, d) stir zone of V100-w1500, e) stir zone of V500-w900, and f) stir zone of V500-w1500 joint.

The energy-dispersive X-ray spectroscopy (EDS) maps in Figure 10 reveal how metal stirring during the FSW process affects the distribution of certain alloying elements in the welded joints. The maps for Ti and B can be related to titanium borides ($TiB_2$), while the Cu map reflects the distribution of Al-Cu precipitates, primarily $Al_2Cu$ [17,18]. As observed in the Ti and B maps, titanium borides are fragmented during the stirring process due to their ceramic nature, leading to a reduction in their size. In contrast, the EDS map for Cu shows a significant change in its distribution after welding. The base material originally shows a uniform distribution of Cu within the Al matrix, with some localized concentration along grain boundaries. However, the stirring action disrupts these localized patterns. In addition, the high temperature reached during the welding process (with a maximum temperature in the 400-500 °C range [48,49]) further promoted the formation of larger Al-Cu precipitates. This particle growth is not observed for titanium borides because of their much higher melting temperature (3230 °C) [18].

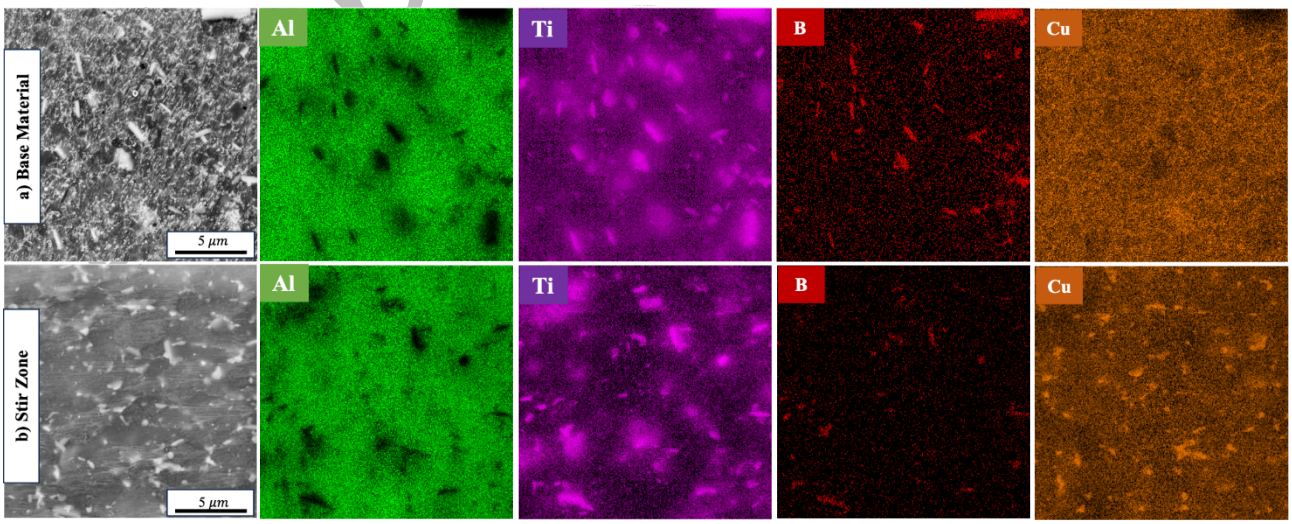


Figure 10. SEM-EDS map showing the distribution of Al, Ti, B, and Cu elements in the a) A20X base material and b) the stir zone of FSW joints.

Figure 11 a) and b) display a Vickers hardness map for the V100-w1500 and V500-w1500 FSW joints in their as-weld state, respectively. As found by other studies [12,50], the hardness of the as-printed A20X is about 115 HV. It can be noted that a large scattering in hardness value of A20X because of the intrinsic porosity and inhomogeneities characterizing the AM microstructure. Notably, the SZ achieves a hardness of 135 HV, similar to what can be achieved after solubilization and aging heat treatment on A20X in [12,47,50]. According to Li et al. [6], the high solidification and cooling rates in the LPBF process of A20X lead to Cu supersaturation within α-Al grains. The amount of Cu in the α-Al matrix can reach 1 - 1.5 wt.% against an overall chemical composition containing about 5 wt.%. Most Cu segregated along the grain boundaries as $Al_2Cu$ precipitates, and the remainder dissolved in the Al matrix as a solid solution during rapid solidification. During FSW, the metal is heated in a 450 - 500 °C range [51] and promotes the precipitation of Cu in solid solution as $Al_2Cu$ precipitates and, hence, an increased joint hardness. It can be noted that a wider hard SZ has been obtained in the sample V500-w1500. This means that, even though it promotes better metal stirring, the higher heat inputs (i.e., higher temperatures) are responsible for microstructural softening. This softening could be attributed to a microstructural overaging caused by a coarsening of $Al_2Cu$ precipitates. From studies about age hardening of A20X [12,47,50], instead, there is no evidence of precipitation of $TiB_2$ and their possible strengthening effect.

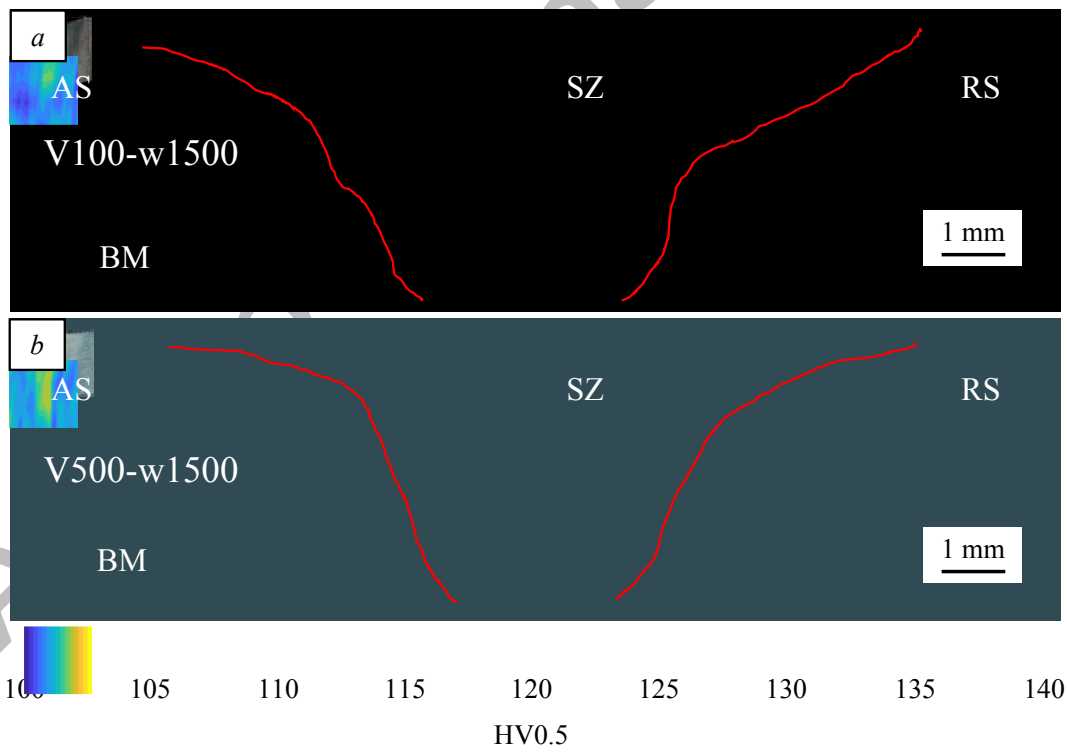


Figure 11. Vickers hardness map of the FSW joints with rotational speed of 1500 rpm and welding speed of a) 100 and b) 500 mm/min.

## 3.3 3D X-ray Computed Tomography

As discussed in the previous paragraph, the metallographic inspection of V100-w900 samples revealed discontinuous tunnel defects throughout the weldment. Therefore, a more in-depth study was carried out

through 3D X-ray Computed Tomography. Two samples, one without and one with the tunnel defect, have been extracted from a V100-w900 weld seam and are shown in Figure 12 a) and b), respectively. The samples with and without the tunnel defect have been labeled “T” and “NT”, respectively. Figure 12 shows the porosity in the NT and T samples after 3D X-ray computed tomography. Such analysis also displays the extent and location of the tunnel defect in the NT sample. Samples NT and T exhibit porosities of 0.38 %vol. (material volume $3.94 \cdot 10^{11}$ µm$^3$, porosity volume $1.49 \cdot 10^{9}$ µm$^3$) and 0.32 %vol. (material volume $3.81 \cdot 10^{11}$ µm$^3$, porosity volume $1.24 \cdot 10^{9}$ µm$^3$), respectively. The mixing and stirring action occurring during the FSW effectively reduces the size of porosities, making the porosity distribution more homogeneous [5]. Figure 12 shows that the SZs of samples NT and T are characterized by pores with volumes below $1.7 \cdot 10^{5}$ µm$^3$, corresponding to an equivalent diameter below 55 µm. Pores are not visible at the joint root, indicating a uniform joint through the plate thickness. The total pores count for samples NT and T were 13975 and 7947, respectively, of which 3323 and 3159 exhibited an equivalent diameter above 55 µm. These larger pores constituted 72 % and 85 % of the overall detected porosity for samples NT and T, respectively. Sample T exhibited a large tunnel defect with a volume of $6.74 \cdot 10^{8}$ µm$^3$. For clarity, this defect has not been included in the computation of the porosity volume for sample T ($1.24 \cdot 10^{9}$ µm$^3$).

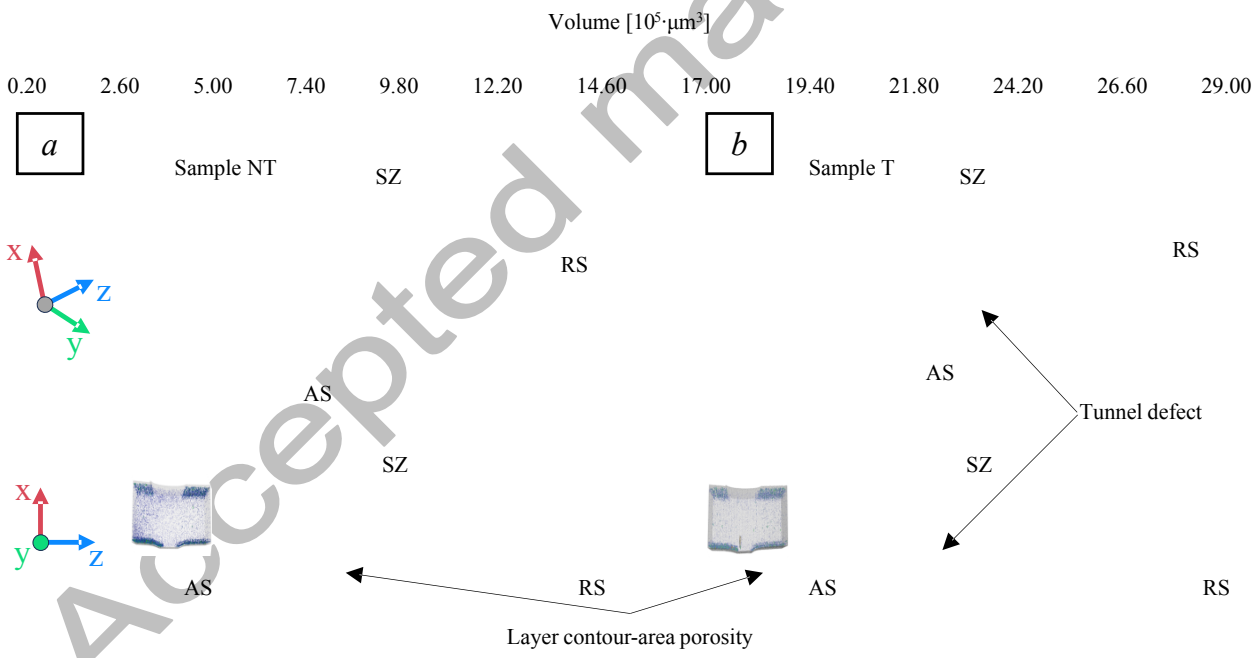


Figure 12. 3D X-ray Computed Tomography: distribution and pore volume in an FSW V100-w900 sample along the weldment in a region a) without and b) with a tunnel defect. The color of the tunnel defect is not referred to the volume color bar.

The images in Figure 13 a) and b) show the plots of porosity sphericity vs. equivalent diameter and maximum diameter, respectively. Both display a hyperbolic correlation, with most pores related to sample T with the tunnel defect. The defect equivalent diameter ranges from 40 to 150 µm, while the maximum diameter ranges from 50 to around 350 µm, with only a few defects of about 450 µm. It can be inferred from the sphericity plots that the most frequent defects are elongated and can be attributed to a lack of fusion. Contrarily, a lower

number of pores exhibit a semi-spherical shape, which might be associated with a gas entrapment occurring during the solidification of the LPBF printed layers [6].

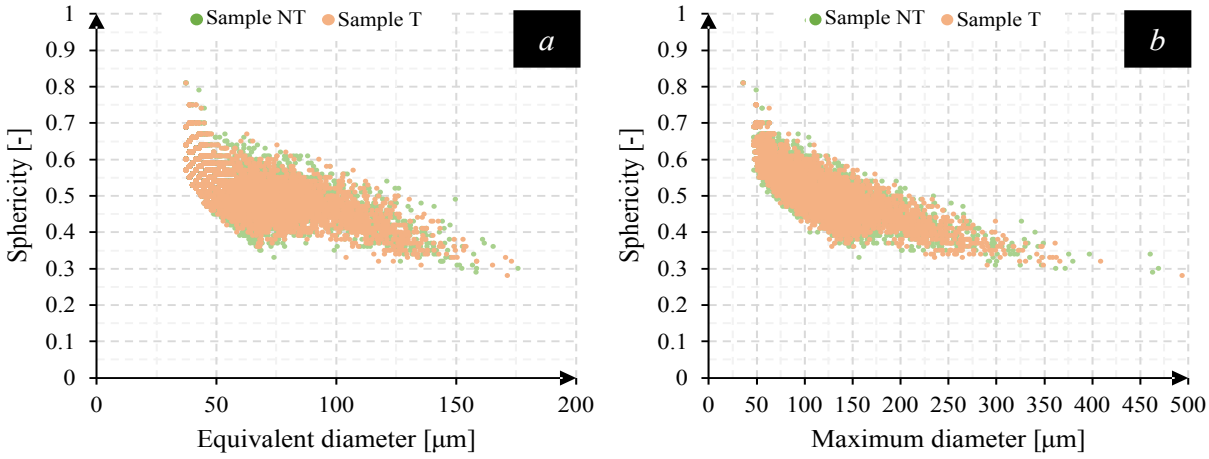


Figure 13. 3D X-ray Computed Tomography of the samples NT and T (V100-w900 sample without and with a tunnel defect, respectively): a) sphericity vs. equivalent diameter and b) sphericity vs. maximum diameter.



### 3.4 Joint tensile strength

Table 3 and Figure 14 show the results of the tensile tests performed on both as-printed and welded A20X samples. The as-printed sample exhibits an average ultimate tensile strength (UTS) of about 385 MPa and an elongation at fracture ($e_f$) of 17 %. These mechanical properties decrease to about 335 MPa and 13 % for the V100-w1500 joints, which did not have a tunnel defect. This defect, instead, limits the mechanical properties of the V100-w900 and V500-w1500 joints. V100-w900 joints show a UTS with a large data scattering related to the occurrence of a discontinuous tunnel throughout the weldment, as found from the 3D X-ray tomographic examination: maximum UTS of 345 MPa and elongation at fracture of 12% in the absence of tunnel (similar to the sound V100-w1500 joint), but lower UTS (about 290 MPa) and elongation at fracture (7 %) when tunnel occurs. The V500-w1500 joints show the lowest mechanical properties (UTS 250 MPa and $e_f$ 6 %) due to the persistent tunnel defects throughout the weld seams. All the samples in Figure 14 show step-like serrations during plastic deformation. Avateffazeli et al. [20] reported similar serrations during tensile testing of as-built A20X produced via LPBF. These serrations are macroscopic evidence of the Portevin-Le Chatelier (PLC) effect that can appear in additively manufactured material. Such a phenomenon is caused by a continuous locking and unlocking of dislocations on solute interstitial atoms and very fine precipitates during deformation [52].

There are few works on FSW of traditional AM aluminum alloys, such as AlSi10Mg and AlSi12. Due et al. [53] reported a 47 % decrease in the UTS of the FSW AlSi10Mg joints from its as-build state, with a drop in UTS from 451 MPA to 240 MPa under optimal welding conditions. Moeini et al. [35] investigated the effect of build direction on the FSW joint of AlSi10Mg alloy. They observed that the UTS of FSW joints was about 25% lower than the as-built material, approximately 300 MPa. Moeini et al. [35] also found that UTS decreased

from around 450 to 300 MPa after joining AlSi12 sheets via FSW. Mirandola et al. [5] have found that the UTS of Scalmalloy® can achieve a mechanical strength like the as-printed condition (about 400 MPa) after an age hardening heat treatment. All these studies have highlighted a noteworthy decrease in the UTS of FSW joints from their as-built counterparts. A20X joints, instead, experienced a mild decrease in mechanical properties after FSW. In the best case, V100-w1500, UTS has reduced by 13 % on average reduction from the as-printed condition. Although more comprehensive microstructural studies are necessary, presumably, the peculiar chemical composition of A20X and the strong grain refining from $TiB_2$ particles could have a noteworthy contribution to such a phenomenon.

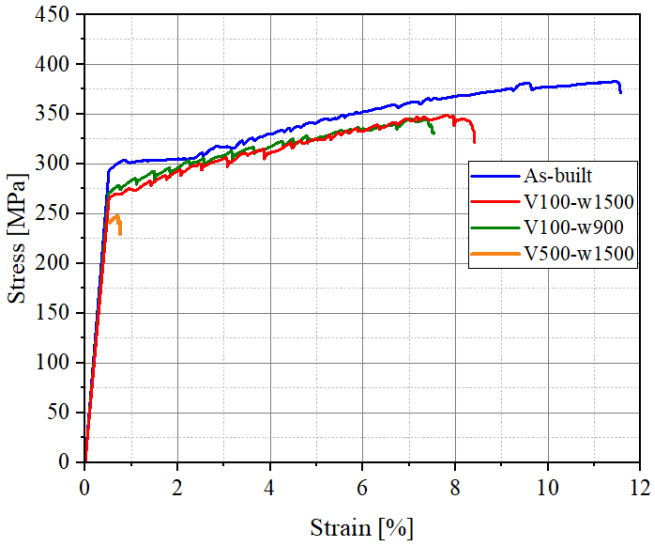


Figure 14. Tensile results for the as-printed and FSW A20X joints.

Table 3 Tensile properties of A20X alloy in as-built and as-weld conditions

| Samples | Yield strength [MPa] | Ultimate strength [MPa] | Elongation to fracture [%] |
|---|---|---|---|
| As-printed | 284 ± 24 | 384 ± 2 | 11.5 ± 1 |
| V100-w900 | 272 ± 5 | 315 ± 27 | 7.5 ± 2 |
| V100-w1500 | 269 ± 1 | 335 ± 19 | 8.5 ± 2 |
| V500-w1500 | 242 ± 7 | 242 ± 7 | 1 ± 0.5 |

A fractographic examination was also carried out to understand the fracture modes of joints at varying welding conditions and the influence of the tunnel defect. The joints V100-w1500, with the highest mechanical properties, failed in the weldment along a pattern going from a region around the bottom border of the SZ through the SZ and the rapid transition region between the SZ and BM at the advancing side with an irregular fracture shape, Figure 15 a). The fracture surfaces do not show evident signs of macroscopic necking like the fracture surface of the as-printed A20X. The same fracture mode has been found for the V100-w900 samples without the tunnel defect, which failed with higher mechanical strengths. The appearance of the fracture surfaces changes when a tunnel defect occurs in the V100-w900 and V500-w1500 joints. This defect is visible on the fracture surfaces shown in Figure 15 b) and c). The crack started from this defect and propagated through a straight pattern along the transition region between the SZ and the BM. This defect reduced the resistance

cross-section of the welded specimen and acted as a stress concentration factor, limiting the overall elongation. The crack patterns of V100-w900 and V500-w900 joints are also shown in the cross-section of the tensile samples in Figure 16 a) and b), respectively. In all these cases, the crack pattern passes through the locations where the tunnel defects were detected through the 3D X-ray tomography. Other studies about FSW of AM Al alloys have reported similar fracture modes, such as the studies of Mirandola et al. [5] for Scalmalloy® and Moeini [35] for AlSi10Mg: fracture patterns along either the SZ or the transition region between the SZ and BM without macroscopic signs of necking.

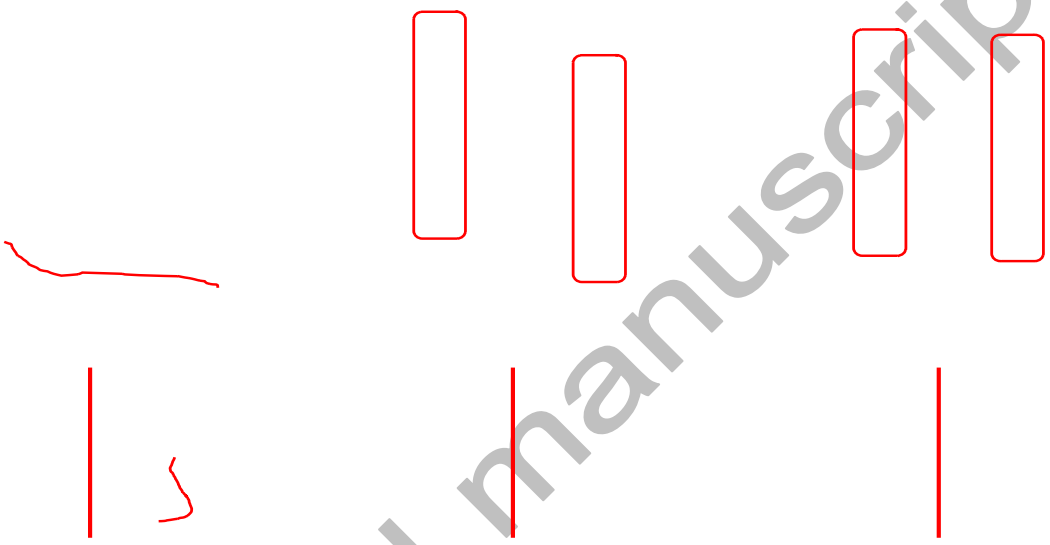

Figure 15. Fracture surface for the a) V100-w1500, b) V100-900, and c) V500-w1500 joints after tensile test.

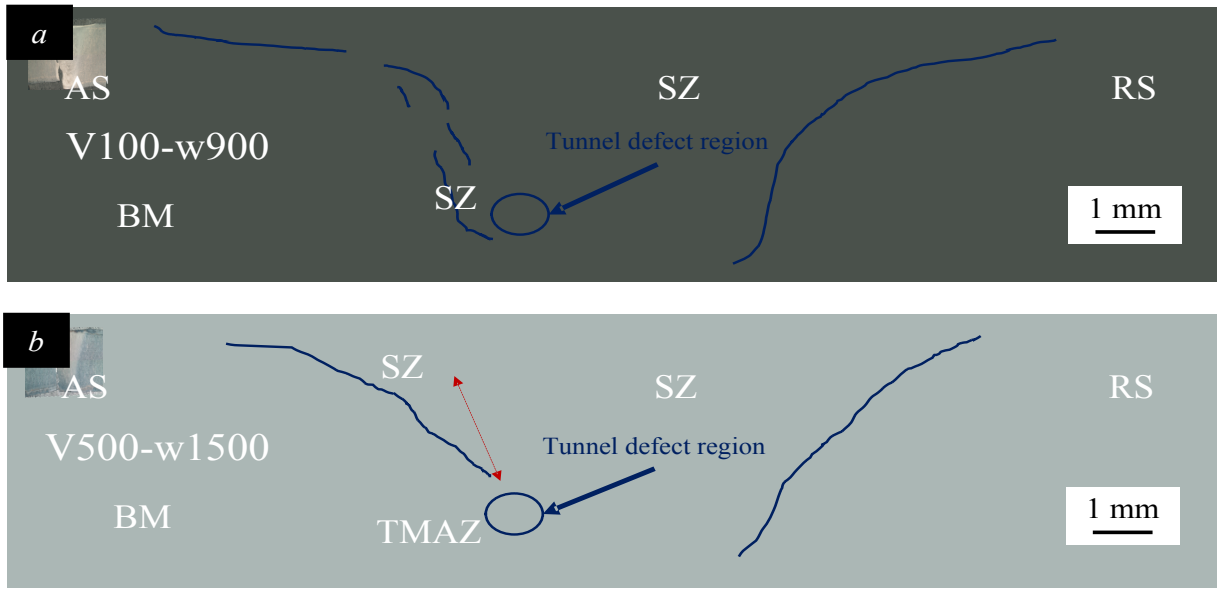


Figure 16. Cross-sections of the failed a) V100-w900 and b) V500-w1500 joints.

Figures 17 and 18 show the fracture surfaces of the as-printed A20X and FSW joints obtained through SEM examination, respectively. The fracture surface of the as-printed A20X shows a typical ductile feature with dimples, Figure 17 a). This agrees with the elongation fracture (11.5 % on average) and the literature [54,55]. The as-printed A20X is also characterized by the occasional presence of some large pores, Figure 17 b), as a direct consequence of the LPBF process. V100-w1500 (Figure 18 a)) and V100-w900 (without tunnel) samples also show ductile fracture modes with the presence of dimples throughout the fracture surface. The lowest elongation of 1% found in the V500-w1500 and some V100-w900 specimens is a consequence of large tunnel defects, Figure 19, and not of an intrinsic brittleness of the metal. It is clear how the metal stirring did not occur properly around the tool pin during FSW, and only some small regions were effectively joined. These joined regions still exhibit a ductile fracture surface even tough with shallower dimples and less pronounced shear lips, Figure 18 b) and c).

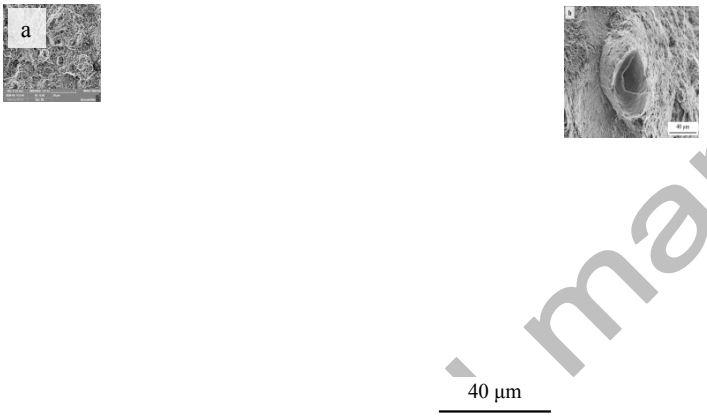


Figure 17. Fracture surface of the tensile samples of as-printed A20X: a) ductile fracture; b) magnification pointing out a pore obtained during LPBF.

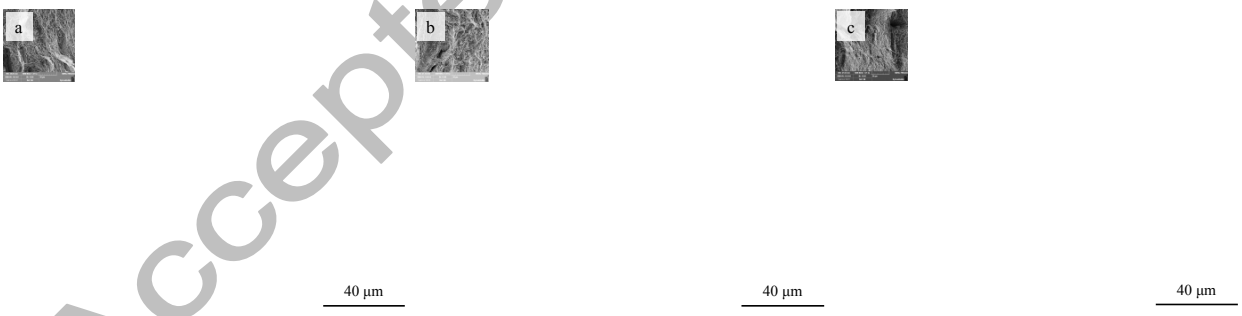


Figure 18. Fracture surfaces of the welded tensile samples outside the tunnel defect, if present: a) V100-w1500 samples (without tunnel defect); b) V100-w900 (with tunnel defect); c) V500-w1500 (with tunnel defect).

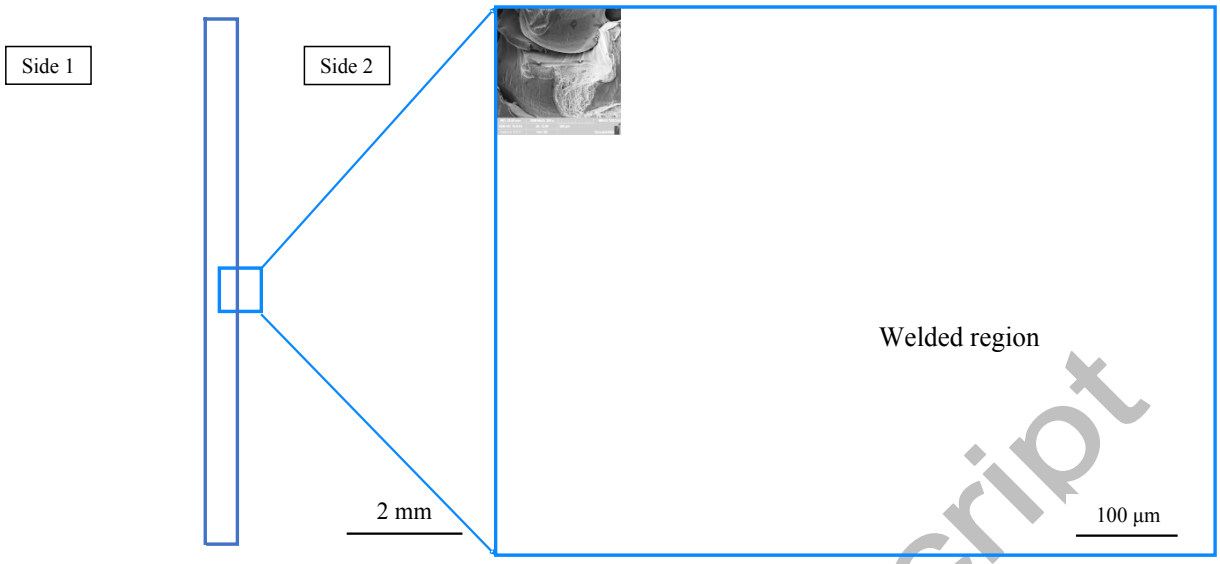


Figure 19. Typical SEM fractographic images of the two broken halves of FSW tensile samples with tunnel defect (SEM images from V500w1500 sample).

## 4. Conclusions

This work reports the findings on the influence of solid-state FSW on the mechanical and microstructural properties of butt joints of advanced A20X alloy produced via LPBF at varying welding conditions. The main results are summarized as follows:

- Regardless of the parameter settings, the welded joints maintain fine and equiaxed grains (average grain size of about 1 µm) in the stir zone without a preferred orientation.
- The joint hardness increases from 115 HV to a maximum of 135 HV, presumably due to local aging caused by the heat input involved in the joining process. Higher heat inputs (V100-w1500 samples) lead to a lower hardness increase, which can be attributed to a slight overaging.
- Insufficient metal stirring in V500-w1500 and V500-w900 samples leads to higher surface roughness and the formation of tunnel defects with a detrimental effect on the joint strength. Tensile strength reduces less than 250 MPa (sound joints over 310 MPa, base metal 375 MPa) and elongation at fracture at 1%.
- The broken tensile samples show fracture patterns throughout the SZ zone or along the region between the BM and the SZ. The SEM fractographic examination reveals that the microscopic fracture mode is always ductile in all the investigated conditions, also in the presence of a tunnel defect.
- EDS analysis reveals that metal stirring during the joining process breaks up the Ti borides and promotes the growth of the Al-Cu precipitates within the stir zone.
- 3D X-ray computed tomography shows that the metal stirring during FSW notably reduces the intrinsic joint porosity of the additively manufactured A20X.

These findings underscore the potential of FSW in joining A20X for applications demanding high mechanical strength and integrity, also emphasizing the need for precise control over welding parameters to mitigate defects and ensure optimal joint performance.

**Statements and Declarations**

**a. Funding** This study was supported by J-Tech@PoliTO, an advanced joining technologies research center at Politecnico di Torino (http://www.j-tech.polito.it/) **b. Conflicts of interest/Competing interests** The authors declare no conflicts of interest or competing interests **c. Availability of data and material** All data generated or analyzed during this study are included within the article **d. Code availability** Not applicable **e. Ethics approval** Compliance with ethical standards **f. Consent to participate** All authors agreed with the consent to participate **g. Consent for publication** All authors have read and agreed to the publication of the paper.

## References

[1] Krochmal M, Rajan ANR, Moeini G, Sajadifar S V., Wegener T, Niendorf T. Microstructural and mechanical properties of AlSi10Mg: Hybrid welding of additively manufactured and cast parts. J Mater Res 2023;38:297–311. https://doi.org/10.1557/S43578-022-00838-1/FIGURES/10.

[2] Mauduit A, Gransac H, Pillot S, Auguste P. A study of AlSi5Cu3Mg alloy produced by laser powder bed fusion: porosity assessment, microstructure, mechanical properties. Mechanics & Industry 2023;24:13. https://doi.org/10.1051/MECA/2023008.

[3] Avateffazeli M, Shakil SI, Hadadzadeh A, Shalchi-Amirkhiz B, Pirgazi H, Mohammadi M, et al. On microstructure and work hardening behavior of laser powder bed fused Al-Cu-Mg-Ag-TiB2 and AlSi10Mg alloys. Mater Today Commun 2023;35:105804. https://doi.org/10.1016/J.MTCOMM.2023.105804.

[4] Paul MJ, Liu Q, Best JP, Li X, Kruzic JJ, Ramamurty U, et al. Fracture resistance of AlSi10Mg fabricated by laser powder bed fusion. Acta Mater 2021;211:116869. https://doi.org/10.1016/J.ACTAMAT.2021.116869.

[5] Mirandola P, Lunetto V, Novel D, Barozzi M, Bellutti P, De Maddis M, et al. Strength and microstructure of friction stir welded additively manufactured Scalmalloy® in as-welded and heat-treated conditions. J Manuf Process 2023;97:1–11. https://doi.org/10.1016/J.JMAPRO.2023.04.051.

[6] Li S, Cai B, Duan R, Tang L, Song Z, White D, et al. Synchrotron Characterisation of Ultra-Fine Grain TiB2/Al-Cu Composite Fabricated by Laser Powder Bed Fusion. Acta Metallurgica Sinica (English Letters) 2022;35:78–92. https://doi.org/10.1007/S40195-021-01317-Y/FIGURES/12.

[7] Ghasri-Khouzani M, Karimialavijeh H, Pröbstle M, Batmaz R, Muhammad W, Chakraborty A, et al. Processability and characterization of A20X aluminum alloy fabricated by laser powder bed fusion. Mater Today Commun 2023;35:105555. https://doi.org/10.1016/J.MTCOMM.2023.105555.

[8] Rometsch PA, Zhu Y, Wu X, Huang A. Review of high-strength aluminium alloys for additive manufacturing by laser powder bed fusion. Mater Des 2022;219:110779. https://doi.org/10.1016/J.MATDES.2022.110779.

[9] Zhang B, Wei W, Shi W, Guo Y, Wen S, Wu X, et al. Effect of heat treatment on the microstructure and mechanical properties of Er-containing Al–7Si–0.6 Mg alloy by laser powder bed fusion. Journal of Materials Research and Technology 2022;18:3073–84. https://doi.org/10.1016/J.JMRT.2022.04.023.

[10] Zhang H, Wang Y, Wang JJ, Ni DR, Wang D, Xiao BL, et al. Achieving superior mechanical properties of selective laser melted AlSi10Mg via direct aging treatment. J Mater Sci Technol 2022;108:226–35. https://doi.org/10.1016/J.JMST.2021.07.059.

[11] Jakkula P, Ganzenmüller G, Gutmann F, Pfaff A, Mermagen J, Hiermaier S. Strain Rate Sensitivity of the Additive Manufacturing Material Scalmalloy®. Journal of Dynamic Behavior of Materials 2021;7:518–25. https://doi.org/10.1007/S40870-021-00298-4/FIGURES/6.

[12] Barode J, Vayyala A, Virgillito E, Aversa A, Mayer J, Fino P, et al. Revisiting heat treatments for additive manufactured parts: A case study of A20X alloy. Mater Des 2023;225:111566. https://doi.org/10.1016/J.MATDES.2022.111566.

[13] Filatov YA, Yelagin VI, Zakharov V V. New Al–Mg–Sc alloys. Materials Science and Engineering: A 2000;280:97–101. https://doi.org/10.1016/S0921-5093(99)00673-5.

[14] Malopheyev S, Mironov S, Kulitskiy V, Kaibyshev R. Friction-stir welding of ultra-fine grained sheets of Al–Mg–Sc–Zr alloy. Materials Science and Engineering: A 2015;624:132–9. https://doi.org/10.1016/J.MSEA.2014.11.079.

[15] Mair P, Braun J, Kaserer L, March L, Schimbäck D, Letofsky-Papst I, et al. Unique microstructure evolution of a novel Ti-modified Al-Cu alloy processed using laser powder bed fusion. Mater Today Commun 2022;31:103353. https://doi.org/10.1016/J.MTCOMM.2022.103353.

[16] Shakil SI, Zoeram AS, Avateffazeli M, Roscher M, Pirgazi H, Shalchi-Amirkhiz B, et al. Ambient-temperature time-dependent deformation of cast and additive manufactured Al-Cu-Mg-Ag-TiB2 (A205). Micron 2022;156:103246. https://doi.org/10.1016/J.MICRON.2022.103246.

[17] Rafieazad M, Fathi P, Nasiri A, Haghshenas M, Mohammadi M. Isotropic corrosion performance of the newly developed L-PBF-A205 aluminum alloy. Mater Lett 2021;291:129541. https://doi.org/10.1016/J.MATLET.2021.129541.

[18] Shakil SI, Zoeram AS, Pirgazi H, Shalchi-Amirkhiz B, Poorganji B, Mohammadi M, et al. Microstructural-micromechanical correlation in an Al–Cu–Mg–Ag–TiB2 (A205) alloy: additively manufactured and cast. Materials Science and Engineering: A 2022;832:142453. https://doi.org/10.1016/J.MSEA.2021.142453.

[19] Ghoncheh MH, Sanjari M, Zoeram AS, Cyr E, Amirkhiz BS, Lloyd A, et al. On the microstructure and solidification behavior of new generation additively manufactured Al-Cu-Mg-Ag-Ti-B alloys. Addit Manuf 2021;37:101724. https://doi.org/10.1016/J.ADDMA.2020.101724.

[20] Avateffazeli M, Carrion PE, Shachi-Amirkhiz B, Pirgazi H, Mohammadi M, Shamsaei N, et al. Correlation between tensile properties, microstructure, and processing routes of an Al–Cu–Mg–Ag–TiB2 (A205) alloy: Additive manufacturing and casting. Materials Science and Engineering: A 2022;841:142989. https://doi.org/10.1016/J.MSEA.2022.142989.

[21] Shamsaei N, Yadollahi A, Bian L, Thompson SM. An overview of Direct Laser Deposition for additive manufacturing; Part II: Mechanical behavior, process parameter optimization and control. Addit Manuf 2015;8:12–35. https://doi.org/10.1016/J.ADDMA.2015.07.002.

[22] Mosallanejad MH, Abdi A, Karpasand F, Nassiri N, Iuliano L, Saboori A. Additive Manufacturing of Titanium Alloys: Processability, Properties, and Applications. Adv Eng Mater 2023;25:2301122. https://doi.org/10.1002/ADEM.202301122.

[23] Bacciaglia A, Ceruti A, Liverani A. Towards Large Parts Manufacturing in Additive Technologies for Aerospace and Automotive applications. Procedia Comput Sci 2022;200:1113–24. https://doi.org/10.1016/J.PROCS.2022.01.311.

[24] Wang W, Meng X, Dong W, Xie Y, Ma X, Mao D, et al. In-situ rolling friction stir welding of aluminum alloys towards corrosion resistance. Corros Sci 2024;230:111920. https://doi.org/10.1016/J.CORSCI.2024.111920.
[25] Zhu Y, Zhou M, Geng Y, Zhang S, Xin T, Chen G, et al. Microstructural evolution and its influence on mechanical and corrosion behaviors in a high-Al/Zn containing duplex Mg-Li alloy after friction stir processing. J Mater Sci Technol 2024;184:245–55. https://doi.org/10.1016/J.JMST.2023.10.019.
[26] Geng Y, Zhou M, Zhu Y, Chen Y, Xin T, Chen G, et al. Regulating microstructure of Mg–Li–Al–Zn alloy for enhancing comprehensive performance through friction stir additive manufacturing. Materials Science and Engineering: A 2024;895:146239. https://doi.org/10.1016/J.MSEA.2024.146239.
[27] Zhang M, Liu FC, Xue P, Zhang H, Wu LH, Ni DR, et al. Fabrication of large-scale steel-aluminum components with homogenously distributed amorphous interfacial layer and enhanced bonding strength using modified friction stir additive manufacturing. J Mater Sci Technol 2024;194:151–66. https://doi.org/10.1016/J.JMST.2024.01.036.
[28] Deutsches Institut für Normung. DIN 50125:2016-12. Testing of metallic materials - Tensile test pieces 2016:17.
[29] ASTM International. Standard Test Methods for Vickers Hardness and Knoop Hardness of Metallic Materials ASTM E92 2017. https://doi.org/10.1520/E0092-17.
[30] Wadell H. Volume, Shape, and Roundness of Quartz Particles. Https://DoiOrg/101086/624298 1935;43:250–80. https://doi.org/10.1086/624298.
[31] Mishra D, Roy RB, Dutta S, Pal SK, Chakravarty D. A review on sensor based monitoring and control of friction stir welding process and a roadmap to Industry 4.0. J Manuf Process 2018;36:373–97. https://doi.org/10.1016/J.JMAPRO.2018.10.016.
[32] Su H, Wu CS, Pittner A, Rethmeier M. Simultaneous measurement of tool torque, traverse force and axial force in friction stir welding. J Manuf Process 2013;15:495–500. https://doi.org/10.1016/J.JMAPRO.2013.09.001.
[33] Mohan DG, Wu CS. A Review on Friction Stir Welding of Steels. Chinese Journal of Mechanical Engineering 2021 34:1 2021;34:1–29. https://doi.org/10.1186/S10033-021-00655-3.
[34] Bozkurt Y. Weldability of metal matrix composite plates by friction stir weldin at low welding parameters. Mater Technol 2011;45:1580–2949.
[35] Moeini G, Sajadifar S V, Wegener T, Rössler C, Gerber A, Böhm S, et al. On the influence of build orientation on properties of friction stir welded Al–Si10Mg parts produced by selective laser melting. Journal of Materials Research and Technology 2021;12:1446–60. https://doi.org/10.1016/J.JMRT.2021.03.101.
[36] Threadgilll PL, Leonard AJ, Shercliff HR, Withers PJ. Friction stir welding of aluminium alloys. International Materials Reviews 2009;54:49–93. https://doi.org/10.1179/174328009X411136.
[37] Heidarzadeh A, Javidani M, Mofarrehi M, Farzaneh A, Chen XG. Submerged Dissimilar Friction Stir Welding of AA6061 and AA7075 Aluminum Alloys: Microstructure Characterization and Mechanical Property. Metals 2021, Vol 11, Page 1592 2021;11:1592. https://doi.org/10.3390/MET11101592.
[38] Scherillo F, Astarita A, Prisco U, Contaldi V, di Petta P, Langella A, et al. Friction Stir Welding of AlSi10Mg Plates Produced by Selective Laser Melting. Metallography, Microstructure, and Analysis 2018;7:457–63. https://doi.org/10.1007/S13632-018-0465-Y/TABLES/2.
[39] Shashi Kumar S, Murugan N, Ramachandran KK. Identifying the optimal FSW process parameters for maximizing the tensile strength of friction stir welded AISI 316L butt joints. Measurement 2019;137:257–71. https://doi.org/10.1016/J.MEASUREMENT.2019.01.023.

[40] Ni Y, Fu L, Shen Z, Liu XC. Role of tool design on thermal cycling and mechanical properties of a high-speed micro friction stir welded 7075-T6 aluminum alloy. J Manuf Process 2019;48:145–53. https://doi.org/10.1016/J.JMAPRO.2019.10.025.
[41] Zettler R, Vugrin T, schmücker M. Effects and defects of friction stir welds. Friction Stir Welding: From Basics to Applications 2010:245–76. https://doi.org/10.1533/9781845697716.2.245.
[42] Liu H, Hu Y, Dou C, Sekulic DP. An effect of the rotation speed on microstructure and mechanical properties of the friction stir welded 2060-T8 Al-Li alloy. Mater Charact 2017;123:9–19. https://doi.org/10.1016/J.MATCHAR.2016.11.011.
[43] Xu W, Wang H, Luo Y, Li W, Fu MW. Mechanical behavior of 7085-T7452 aluminum alloy thick plate joint produced by double-sided friction stir welding: Effect of welding parameters and strain rates. J Manuf Process 2018;35:261–70. https://doi.org/10.1016/J.JMAPRO.2018.07.028.
[44] Verma M, Ahmed S, Saha P. Challenges, process requisites/inputs, mechanics and weld performance of dissimilar micro-friction stir welding (dissimilar μFSW): A comprehensive review. J Manuf Process 2021;68:249–76. https://doi.org/10.1016/J.JMAPRO.2021.05.045.
[45] Sauvage X, Dédé A, Muñoz AC, Huneau B. Precipitate stability and recrystallisation in the weld nuggets of friction stir welded Al-Mg-Si and Al-Mg-Sc alloys. Materials Science and Engineering A 2008;491:364–71. https://doi.org/10.1016/J.MSEA.2008.02.006.
[46] Avateffazeli M, Khan MF, Shamsaei N, Haghshenas M. Microstructure, Mechanical, and Fatigue Properties of a Laser Powder Bed Fused Al-Cu-Mg-Ag-Ti-B (A205) Alloy 2022. https://doi.org/10.26153/TSW/44159.
[47] Avateffazeli M, Shakil SI, Khan MF, Pirgazi H, Shamsaei N, Haghshenas M. The effect of heat treatment on fatigue response of laser powder bed fused Al-Cu-Mg-Ag-TiB2 (A20X) alloy. Mater Today Commun 2023;35:106009. https://doi.org/10.1016/J.MTCOMM.2023.106009.
[48] Jamshidi Aval H. Effect of heat input in dissimilar friction stir welding of A390-10 wt.% SiC composite–AA2024 aluminum alloy. Archives of Civil and Mechanical Engineering 2024 24:3 2024;24:1–15. https://doi.org/10.1007/S43452-024-00957-Y.
[49] Acharya U, Yadava MK, Banik A, Saha SC, Saha Roy B. Effect of Heat Input on Microstructure and Mechanical Properties of Friction Stir Welded AA6092/17.5 SiCp-T6. J Mater Eng Perform 2021;30:8936–46. https://doi.org/10.1007/S11665-021-06122-3/FIGURES/13.
[50] Kulkarni A, Srinivasan D, Kumar S, Kumar P, Jayaram V. Precipitate evolution and thermal stability of A205 fabricated using laser powder bed fusion. J Mater Sci 2023;58:2310–33. https://doi.org/10.1007/S10853-023-08163-6.
[51] Ren JG, Wang L, Xu DK, Xie LY, Zhang ZC. Analysis and modeling of friction stir processing-based crack repairing in 2024 aluminum alloy. Acta Metallurgica Sinica (English Letters) 2017;30:228–37. https://doi.org/10.1007/S40195-016-0489-8/FIGURES/13.
[52] Nie X, Zhang H, Zhu H, Hu Z, Qi Y, Zeng X. On the role of Zr content into Portevin-Le Chatelier (PLC) effect of selective laser melted high strength Al-Cu-Mg-Mn alloy. Mater Lett 2019;248:5–7. https://doi.org/10.1016/J.MATLET.2019.03.112.
[53] Du Z, Tan MJ, Chen H, Bi G, Chua CK. Joining of 3D-printed AlSi10Mg by friction stir welding. Welding in the World 2018;62:675–82. https://doi.org/10.1007/S40194-018-0585-7.
[54] Barode J, Vayyala A, Aversa A, Yang L, Mayer J, Fino P, et al. Natural and artificial aging behaviour of Al-Cu-Mg-Ag-Ti-B (A205) alloy processed by laser powder bed fusion: Strengthening mechanisms and failure analysis. Mater Today Commun 2024;39:108978. https://doi.org/10.1016/J.MTCOMM.2024.108978.

[55] Karimialavijeh H, Ghasri-Khouzani M, Chakraborty A, Pröbstle M, Martin E. Direct aging of additively manufactured A20X aluminum alloy. J Alloys Compd 2023;968:172071. https://doi.org/10.1016/J.JALLCOM.2023.172071.